

Low Cost Compact Nanosecond Pulsed Plasma System for Environmental and Biomedical Applications

Muhammad Arif Malik¹ · Karl H. Schoenbach¹ ·
Tarek M. Abdel-Fattah^{2,3} · Richard Heller^{1,4} ·
Chunqi Jiang^{1,5}

Received: 25 July 2016 / Accepted: 9 September 2016
© Springer Science+Business Media New York 2016

Abstract Nanosecond pulsed non-thermal atmospheric-pressure plasmas are promising for numerous applications including air and water purification, ozone synthesis, surface sterilization, material processing, and biomedical care. However, the high cost of the nanosecond pulsed power sources has hindered adaptation of the plasma-based technologies for clinical and industrial use. This paper presents a low cost (<100US\$) nanosecond pulsed plasma system that consists of a Cockcroft–Walton high voltage charging circuit, a compact nanosecond pulse generator using a spark gap as switch, and a plasma reactor. The nanosecond pulse power source requires only a 12 V DC input, hence is battery operable. Through the optimization of the experimental parameters, pulses with a peak voltage >10 kV, a 3 ns rise time (10 to 90 %), and a 10 ns pulse duration (full width at half maximum) at a pulse repetition rate of up to 500 Hz were achieved in the present study. It has been successfully tested to power three different plasma reactors to form pulsed corona discharges, dielectric barrier discharges, and sliding discharges. The energy efficiency of such a nanosecond pulsed sliding discharge system was assessed in the context of ozone synthesis using air or oxygen as the feed gas, and was found comparable to a previously reported non-thermal plasma system that used commercial high voltage pulsed power sources. This study demonstrated that this low-cost nanosecond pulsed power source can

✉ Muhammad Arif Malik
mmalik@odu.edu; MArifMalik@gmail.com

¹ Frank Reidy Research Center for Bioelectronics, Old Dominion University, 4211 Monarch Way, Suite 300, Norfolk, VA 23508, USA

² Department of Molecular Biology and Chemistry, Christopher Newport University, Newport News, VA 23606, USA

³ Applied Research Center, Thomas Jefferson National Accelerator Facility, Newport News, VA, USA

⁴ School of Medical Diagnostic and Translational Sciences, College of Health Sciences, Old Dominion University, Norfolk, VA, USA

⁵ Department of Electrical and Computer Engineering, Old Dominion University, Norfolk, VA 23529, USA

prove to be an energy efficient and simple supply to drive various non-thermal atmospheric-pressure plasma reactors for environmental, medical and other applications.

Keywords Cockcroft–Walton voltage multiplier · Nanosecond pulsed power · Non-thermal plasma · Ozone synthesis · Energy efficiency

Introduction

Nanosecond pulsed non-thermal atmospheric pressure plasmas have been used for a number of applications [1, 2]. The applications include air purification, i.e., removal of: toxic volatile organic compounds [3, 4], odor causing compounds [5–9], acid gas like nitrogen oxides from flue gas [10–13], air born viruses, bacteria and allergens [14–17]; water treatment [18–21]; ozone synthesis from air or oxygen [22–24]; plasma medicine including wound decontamination [25–27], nitric oxide inhalation therapies [28–30], cancer treatment [31–33], etc.

Comparative studies show that pulsed high voltage is, in general, more energy efficient than AC or DC high voltage for driving plasma chemical reactions, e.g., for ozone synthesis [34, 35], destruction of toxic volatile organic compounds [36, 37], nitric oxide removal [38, 39], etc. Further, short pulses of a few nanoseconds duration and short rise time (few nanoseconds) are, in general, more energy efficient for driving chemical reactions than longer duration pulses with slower rise times. A recent comparison study of 5 and 140 ns pulsed plasma jets showed enhanced $O(^3P)$ production by the shorter voltage pulse with a faster rise time [40]. Other comparison studies also showed enhanced performance for nitric oxide removal [41–43] using ultrashort pulsed plasmas [42–44]. It is known that pulsed application allows higher values of reduced electric fields E/n (where E is the electric field and n the neutral density) present at the electrode(s) during the discharge initiation comparing to AC or DC power schemes [35]. The use of shorter rise times (e.g. few ns or subnanosecond) will further increase the E/n upon breakdown [40]. Since the electric field-induced electronic processes play critical roles in plasma chemistry, selectivity and high efficiency of desired products can be achieved with enhanced ionization during discharge initiation and the associated highly non-equilibrium electron energy distribution function of the short pulsed plasma.

The recent development of power electronics has made possible tabletop-sized high voltage nanosecond pulsed power sources [45]. However, the cost for solid-state based high voltage pulse generators is typically high (>US\$10,000) mainly due to the limited availability of high voltage fast solid-state switches and the complexity of the supporting circuitry required to achieve both high voltage and fast response. In addition, the power delivery from these pulsed power sources to the plasma load is sometimes challenging due to the strict requirement of impedance matching between the source output, the transmission line, and the load. We demonstrate here a simple, robust, low cost (<US\$100) pulsed power system using a gas-discharge-based switch (spark gap) for nanosecond pulsed plasma generation. This nanosecond high voltage pulsed power source requires only a 12 V DC input, using a 12 V DC power supply or a 12 V battery. It is based on a Cockcroft–Walton Voltage Multiplier circuit [46]. The circuit was reported by Greinacher [47] and improved by Cockcroft and Walton [48] and it is still being developed for different high voltage applications [49–52]. High voltage pulses, >10 kV having 3 ns rise

time (10 to 90 %), 10 ns pulse duration (full width at half maximum) at a pulse repetition rate of up to 500 Hz were achieved in the present study. The simplicity of the pulse generator circuit allows easy modification of the pulse parameters for a variety of experimental studies. Since the discharge in the switch does not have sufficient time to thermalize due to the short duration of the voltage pulse (~ 10 ns), the discharge remains at a transient spark mode where the heating of the spark-gap electrodes is minimal and so is the erosion [53]. This increases the life of the switch significantly. Importantly, the pulse parameters including the pulse duration, voltage amplitude and pulse repetition rate can all be easily changed with a small adjustment of the circuit components such as the charging capacitance, the spark-gap distance and the number of stages in the Cockcroft–Walton voltage multiplier. The flexibility of adjustment of the nanosecond pulse parameters is an advantage in addition to the low-cost for this pulse power system that will allow researchers in bioelectrics, plasma medicine, and plasmas chemistry to conduct systematic and fundamental studies of these fields of nanosecond stimulated physical and biological effects.

This simple system has been successfully used to power pulsed corona discharge, sliding discharge, shielded sliding discharge, surface dielectric barrier discharge and plasma jet using the respective plasma reactors that were employed in our previously reported studies [30, 54, 55]. Ozone synthesis using the nanosecond pulsed power source and a shielded sliding discharge system is demonstrated in this study as a representative plasma chemical synthesis system, whose energy efficiency was assessed against the previously reported non-thermal plasma systems using commercially available pulsed power supplies.

Experimental

Figure 1 shows the system comprising: a 12 V, 0–1A DC charger; a DC to high voltage AC inverter (3 kV, 20 mA, Plasma Power Generator, MINIMAX30); a 4-stage Cockcroft–Walton Voltage Multiplier; a 3.33 M Ω current limiting resistor (R_{CH}); a charging capacitor (C_{CH}); a spark gap switch; and a load. The Cockcroft–Walton voltage multiplier has two high voltage capacitors (1nF, 20 kV, Ceramic Disk Capacitor) and two diodes (16 kV, 5 mA, VG16/20 High Voltage Rectifier) per stage. The current-limiting resistor, also called a charging resistor, separates the low-current DC charging circuit from the high peak

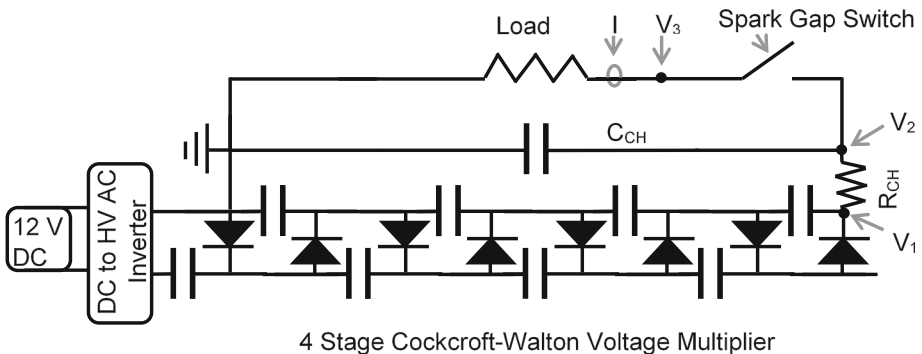


Fig. 1 Schematics of the experimental setup

current discharging circuit. The charging capacitors (1nF, 20 kV or 0.5nF, 10 kV ceramic disk capacitors) are arranged in series and/or parallel combinations to obtain the desired overall capacitance. For calibration and load matching, a 500 Ω carbon composite resistor was used at the load replacing the plasma reactor or in parallel with it.

The charging capacitor was discharged through a spark gap switch made of two stainless steel rods of 6 mm diameter having hemispherical shaped ends and a gap between them which is adjustable from 0 to 7 mm. The pulsed power supply can be enclosed in a 4 cm \times 4 cm \times 18 cm acrylic box. Pulsed DC high voltage pulses of positive polarity were delivered to the load. The spark gap distance was kept at 3.2 mm and the input voltage at 12 V in this study unless mentioned otherwise. The life of the spark gap was measured to be in excess of 10^7 pulses without major changes in the delivered voltage waveform. The total cost of all the components is estimated to be less than \$100 (Source: Information Unlimited, Weblink: <http://www.amazing1.com>).

For ozone synthesis, two sliding discharge electrode assemblies shown in Fig. 2 were employed. The electrodes were made of 50 μ m thick aluminum foil (ALF200L from Intertape Polymer Groups, USA). In one assembly, the high voltage electrode (anode) had three strips measuring 118 mm \times 1.6 mm interconnected at the top. The counter-electrode (cathode at ground potential) had four strips of the same dimensions sandwiching the anode, interconnected at the base. The inter-electrode gap was 6.4 mm. The electrodes were glued to a dielectric sheet made of soda glass measuring 2.4 mm \times 76 mm \times 152 mm. A second rectangular anode (also called shield) measuring 139 mm \times 51 mm was glued on the opposite side of the dielectric, covering the inter-electrode gaps. This electrode assembly is referred to as the three high voltage strips (3HVS) assembly. A second electrode assembly similar to the above but with five high voltage strips (5HVS) each measuring 122 mm \times 1.6 mm sandwiched between six cathode strips with an inter-electrode gap of 3.2 mm was also employed for ozone synthesis. The electrode assembly was converted into a discharge chamber (plasma reactor) by adding a second dielectric sheet carrying only the rectangular cathode (shield) on the outer side and separated by a

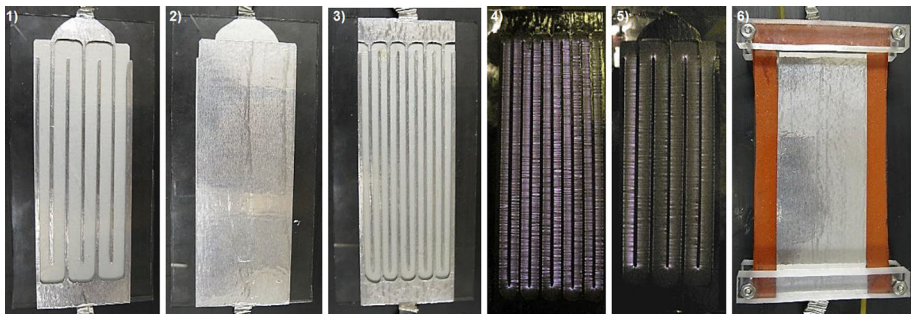


Fig. 2 Images of electrode assemblies, *from left to right*: 1 front view of electrode assembly having three high voltage strips (3HVS) interconnected at *top*, sandwiched between four cathode strips interconnected at *bottom* and a rectangular shield (cathode) covering the gap between the electrodes on opposite side of the dielectric, 2 the opposite (back) side view of the 3HVS electrode assembly showing the rectangular cathode, 3 a similar electrode assembly having five high voltage strips (5HVS), 4 image of plasma in the 5HVS, 5 image of the plasma in 3HVS, 6 discharge chamber having 3HVS or 5HVS at the *bottom*, a second dielectric having the rectangular cathode on the outer side separated by a silicon spacer, gas inlet/outlet at *top* and *bottom* corners, and high voltage and ground potential connections at the *top* and *bottom* center. Cathode strips and the rectangular cathode (shield) on the outer side of the discharge chamber are kept at ground potential

silicon spacer. The silicon spacer was made from a silicon rubber sheet measuring 6 mm × 76 mm × 152 mm, from which a 6 mm × 51 mm × 127 mm block (defining inside dimensions of the reactor) was cut from the middle. Gas inlet and outlet were nylon tubes of 2.4 mm ID and 3.2 mm OD extending through holes on opposite corners of the top and bottom sides of the spacer allowing gas to flow parallel to the electrode strips.

A Tektronix P6015A voltage probe, Pearson Electronics Current Monitor (Model 6585), and Tektronix TDS 2024C oscilloscope were used to measure the temporal development of voltage and current. The energy per pulse (E_P) is the time integral of power over the full width of the pulse:

$$E_P = fV_3 I dt, \quad (1)$$

where V_3 and I are the discharge voltage at the load and the current, respectively. The power dissipated at the load (W_L) is the product of E_P and the pulse repetition rate (f), i.e., $W_L = E_P f$. Experiments were carried out at room temperature (25 °C) and atmospheric pressure. Dry air and/or pure oxygen were supplied from a pressurized gas cylinder at an overall flow rate measured in liters per minute (L/min). Ozone was analyzed based on the UV absorption technique using an ozone analyzer (gFFOZ, IN USA, Inc., Needham, MA) and is expressed in grams per normal cubic meter (g/Nm^3) and in parts per million by volume (ppmv). The specific input energy (SIE) is expressed in Joules dissipated in the discharge per liter of gas treated (J/L) and the energy yield (EY) in grams of ozone produced per kilowatt-hours of energy dissipated in the discharge chamber (g/kWh). The calculations are detailed elsewhere [24]. Time integrated images of multiple discharge events (about one hundred consecutive discharge events) showing top views of the electrode assemblies were obtained with a digital camera, Canon 4 × Optical zoom, 12.1 mega Pixels.

Results and Discussion

With 12 V DC input, the DC/AC inverter puts out ~50 kHz, ~2.5 kV sinusoidal signals [50]. The AC voltage (V_s) is then rectified and the amplitude is amplified for nearly two times by each stage of the Cockcroft–Walton circuit [46, 56]. The maximal output DC voltage (V_{max}) can be estimated using the following expression [56]:

$$V_{max} = 2nV_s - (I_c/fC)(2n^3/3 + n^2/2 - n/6), \quad (2)$$

where we have $f = 50$ kHz for the frequency of the AC voltage, $C = 1$ nF as the capacitance used in the Cockcroft–Walton circuit, $n = 4$ for the number of stages, and I_c is the charging current provided by high voltage DC charging circuit connected to the discharge system. This relation shows that the high voltage multiplier circuit can provide nearly a 20 kV output if the load impedance of the circuit is infinite or the current I_c is zero, respectively. In reality, it is never the case. In fact, the charging current I_c highly depends on the load, such that the DC output provided to the charging capacitor changes with the total impedance of the charging load. For this study, the maximal DC voltages between 12 and 18 kV were measured under different load conditions.

The Cockcroft–Walton circuit charges the charging capacitor, which, in turn, is discharged through the spark gap switch delivering the high voltage pulse to the load. The spark gap switch is self-regulated by the gap distance between the electrodes. The following sections detail the effects of the circuit components including the charging resistor

and capacitor on nanosecond pulse generation as well as the ozone synthesis. In addition, the energy balance is presented to evaluate the system efficiency.

Effect of Charging Resistor

Waveforms of the typical voltage across a $500\ \Omega$ load resistor and the corresponding current with and without a charging resistor are shown in Fig. 3. When the output of the DC charging output was directly connected to the charging capacitor without using a charging resistor, the peak voltage was 12.5 kV, the voltage rise time (10–90 %) was 20 ns, the pulse width, i.e., full width at half maximum (FWHM) was 200 ns, the $1/e$ time constant was 360 ns, as shown in Fig. 3a. After applying a $3.3\ \text{M}\Omega$ charging resistor, the voltage across the load decreased to 9.5 kV, with a voltage rise time (10–90 %) of 3 ns, pulse width (FWHM) of 50 ns, $1/e$ time constant of 65 ns, as shown in Fig. 3b.

Note that although the peak voltage across the $500\ \Omega$ load resistor is lower for the case with the charging resistor applied compared to without the use of the charging resistor, the DC output from the high voltage multiplier should be comparable or greater as the charging current I_c is either negligibly small for both or less for the former. Based on our measurements (detailed in later sections), the charging current can be estimated to be on the order of 1 mA, which would result in a relatively large potential drop across the charging resistor, e.g. $\sim 3\ \text{kV}$. This agrees well with the difference in the peak voltages of the two cases with and without the charging resistor.

The characteristic difference of the voltage and current waveforms for the two cases is due to the equivalent charging capacitance in the discharge circuit. Without using the charging resistor, the total capacitance from the output of the Cockcroft–Walton circuit is in parallel to the charging capacitor, which results in an equivalent total capacitance of $0.5\ \text{nF} + 0.1\ \text{nF} = 0.6\ \text{nF}$. Discharging the total equivalent capacitance via a $500\ \Omega$ resistor leads to an exponential decay with a $1/e$ time constant of 300 ns. When the capacitors in the Cockcroft–Walton circuit are separated from the discharge circuit by means of the large charging resistor, the only capacitance which contributes to the pulse is $C_{\text{CH}} = 100\ \text{pF}$. Discharging of the capacitor via the $500\ \Omega$ resistor causes an exponential decay with a $1/e$ time constant = 50 ns. The estimated decay times are about 80 % of the measured decay time. Considering other parasite capacitances and inductances that the circuit may have, the 20 % discrepancy is reasonable for our analysis.

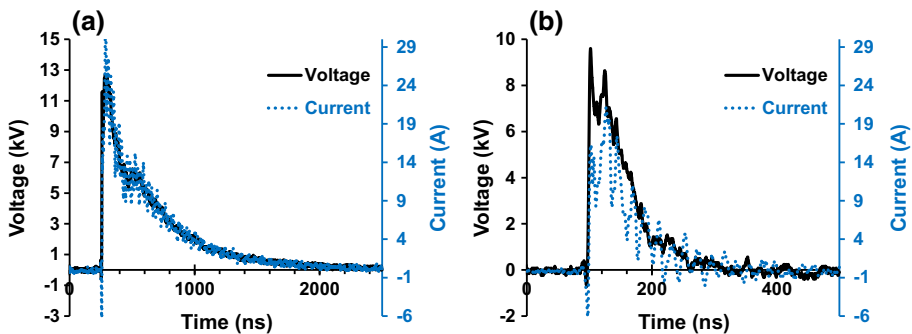


Fig. 3 Typical voltage (V_3) and current waveforms at the load without charging resistor (a) and with charging resistor ($R_{\text{CH}} = 3.3\ \text{M}\Omega$) installed (b). Conditions: 12 V input, load = $0.5\ \text{k}\Omega$ resistor, and $C_{\text{PF}} = 100\ \text{pF}$

It can be concluded from this section that the pulse duration can be defined by the value of the charging capacitance (C_{CH}). A charging resistor or an inductor should be used to separate the high peak current discharging circuit from the low current charging circuit.

Energy Balance

Typical voltage at V_1 , V_2 , and V_3 points in Fig. 1 and current waveforms are shown in Fig. 4. When the spark-gap switch breaks down at a given voltage V_2 , e.g. 12 kV, the energy stored in the charging capacitor is delivered to the load (either a resistor or plasma reactor) at a current, I . The current has a maximum of about 14A and a pulse width (FWHM) of 60 ns. The voltage and current waveforms are mostly in phase, which is consistent with the mostly resistive impedance of the load. The energy deposited per pulse in the load resistor (E_P) is 3.7 mJ. At a frequency of 500 Hz, as calculated from the average time between pulses, the electrical power is 1.9 W. Considering that the input power (12 V times 0.9A) is 10.8 W, this is 17 % of the total power.

The data in Fig. 4 show clearly that the switch is not perfect. Its voltage, i.e., V_2-V_3 , and correspondingly, its resistance, decreases rather slowly, over a time of 40 ns. It reaches a minimum of about 1.5 kV at a current of approximately 15A, corresponding to a resistance of $\sim 100 \Omega$. After that it rises slowly again (recovery phase). The total energy dissipated in the spark gap switch per pulse (E_{SG}) is 1.9 mJ which is calculated using the following integral integrated over the pulse duration:

$$E_{SG} = \int ((V_2 - V_3) * I) dt \tag{3}$$

It corresponds to close to 1 W (for a repetition rate of 500 Hz), i.e., about 10 % of the input power.

A major portion of the remaining power is likely to be dissipated in the charging resistor. In order to determine the power loss in the charging resistor we need to look at the voltage traces V_1 and V_2 over a longer timescale, the time between pulses. The difference of V_1 and V_2 gives the voltage across the charging resistor. Since we know the resistance of this resistor, R_{CH} , we can calculate the power dissipated in the resistor. The dissipated

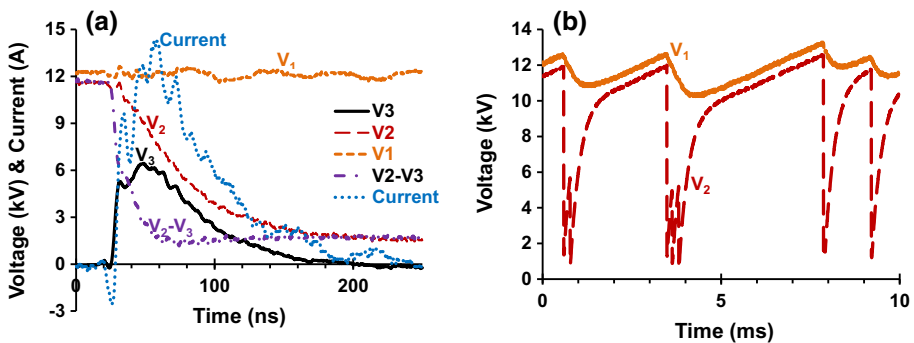


Fig. 4 Typical voltage waveforms of the output of the Cockroft–Walton circuit (V_1), of the pulse forming capacitor (C_{CH}) (V_2), and across the resistive load (V_3), all of which refer to a common ground; and the current waveform through the resistive load (I). The corresponding measuring points were indicated in Fig. 1. Conditions: 12 V input, load = 0.5 k Ω resistor, and C_{CH} = 100pF

energy in the charging resistor (E_{CH}) is given by the power dissipation integrated over time:

$$E_{CH} = \int [(V_1 - V_2)^2 / R_{CH}] dt \quad (4)$$

When integrated over 10 ms the energy dissipated over four events, as shown in Fig. 4b, is 37 mJ. Extrapolating this to 1 s gives us a total value of 3.7 W i.e., ~34 % of the input power.

The resistance of each voltage probe (R_{VP}) was 100 M Ω . Being a high resistance value, the energy loss in it remains negligible in the case of V_3 because the voltage stays on for 1/10,000 fraction of the total time. However, the energy loss in the voltage probes is not negligible in the case of V_1 and V_2 as shown in the following calculations. The energy dissipated in the resistance of the voltage probe (E_{VP}) was calculated using the following integral:

$$E_{VP} = \int [(V)^2 / R_{VP}] dt, \quad (5)$$

where V is either V_1 or V_2 and R_{VP} is 100 M Ω . Integrated over 10 ms, the energy dissipated over four events, as shown in Fig. 4b, is 14 mJ for V_1 and 10 mJ for V_2 . Extrapolating these to 1 s gives us a total power of 1.4 W for V_1 and 1 W for V_2 , corresponding to ~13 and ~9 % of the total input power, respectively.

All power losses which are accounted for in this study are approximately 80 % of the total power provided. They are mainly due to Joule energy losses in the resistive part of the circuit. That includes the resistive load of the fixed resistance, which is used in determining the efficiency of the pulse generator. The discrepancy between power supplied and power dissipated might be due to the losses in the Cockcroft–Walton circuit, particularly in the dc to ac inverter. When the load is an electrode assembly for plasma generation, rather than a load resistor as in the following experiments, a part of the electrical energy is used in driving the plasma chemical reactions. The remaining electrical energy part ends up heating the plasma.

Figure 4b shows that instead of single pulses equally spaced in time, bursts of pulses in a discharge event can happen. Single pulses almost equally spaced in time were obtained by increasing the capacitance of the pulse forming capacitor as described in the following sections.

Effect of the Charging Capacitance

The load resistor R_L in Fig. 1 was replaced with a sliding discharge electrode assembly 5HVS, keeping all other components the same. The capacitance of the electrode assembly was ~90pF. It should be mentioned that this capacitance was measured without the discharge and it might change significantly during the discharge event. For the charging capacitance (C_{CH}) of 75pF, the representative voltage and current waveforms are shown in Fig. 5a, b. Peak voltage of the pulse was 5.5 kV, voltage rise time (10–90 %) was 3 ns, pulse width (FWHM) was 11 ns, energy per pulse dissipated in the plasma was 3.1 mJ, and that dissipated in the spark gap was 6.7 mJ.

Figure 5b shows that the voltage pulses across the plasma reactor are not evenly spaced in time, and occasionally shorter-duration pulses with much lower amplitudes are superimposed on the longer pulses. This statistical behavior of the pulse waveforms, indicating

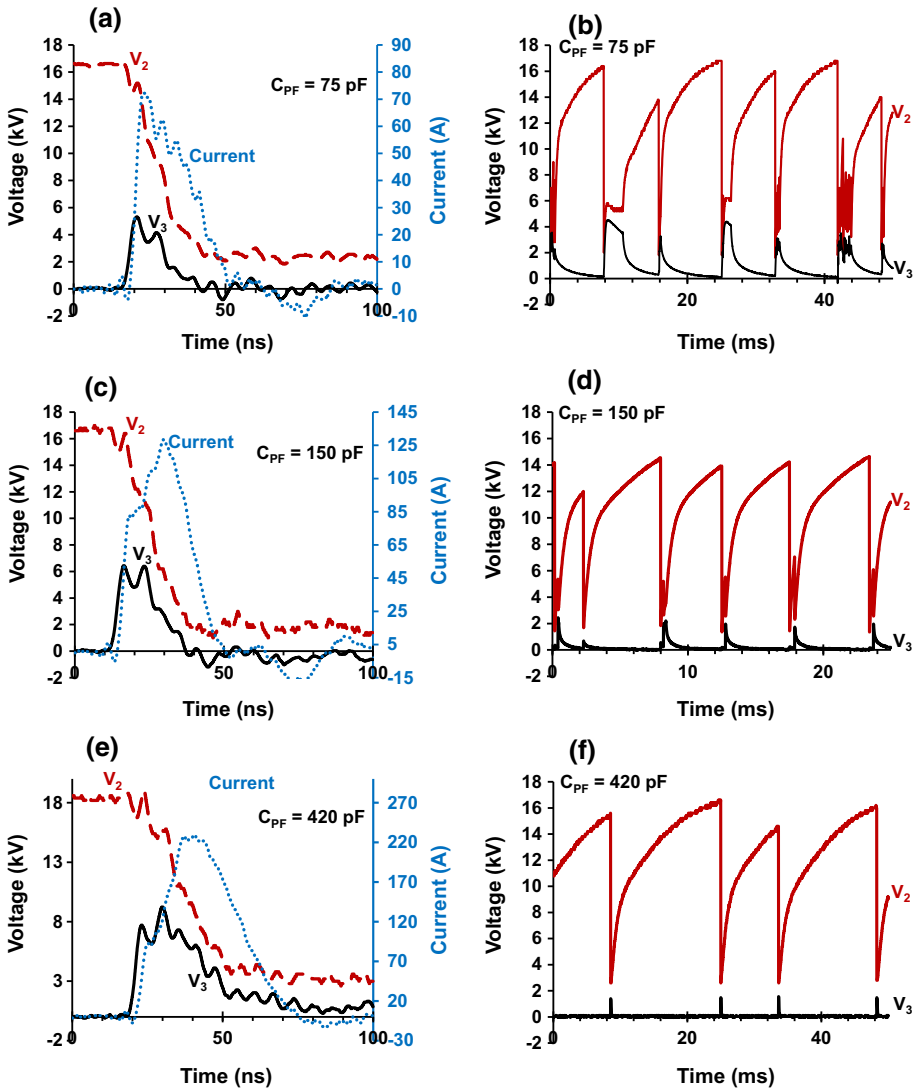


Fig. 5 Typical voltage waveforms at the pulse forming capacitor (C_{PF}) (V_2), and at the load (V_3), referring to the common ground, and the current waveform measured through the load (I) for different pulse forming capacitances (C_{PF}). Conditions: 12 V input, load = 5HVS electrode assembly

an unstable energy delivery, is due to the operation mode of the spark-gap switch, during which the switch is not fully closed.

For the charging capacitance being increased to 150pF, the resulting current and voltage waveforms are shown in Fig. 5c, d. The peak voltage increased to 6.5 kV, voltage rise time (10–90 %) remained at 3 ns, pulse width (FWHM) increased to 13 ns, the energy per pulse dissipated in the plasma increased to 7.5 mJ, and that dissipated in the spark gap increased to ~ 11 mJ. Figure 5d shows that the burst of pulses in each discharge event decreased significantly.

Figure 5e, f show that increasing the charging capacitance further to 420pF caused a peak voltage increase to 9.2 kV, voltage rise time (10–90 %) remained at 3 ns, pulse width (FWHM) increased to 22 ns, energy per pulse dissipated in the plasma increased to 30 mJ, and that dissipated in the spark gap increased to 24 mJ. Note that the energy dissipated in the sliding discharge was more than that dissipated in the spark gap switch in the case of the highest charging capacitance. An important result of the increase in the charging capacitance from 75 to 420pF is that the voltage waveforms become more repeatable and the superimposed shorter-duration pulses are eliminated with the switch operating at a fully closed mode. This is evident from comparing Fig. 5f with b. With the charging capacitance increasing, the energy stored in the charging capacitor becomes sufficient to fully close the switch and allow the transition of the plasma of the spark-gap from statistical initiation to a highly conductive mode.

With the increase of the pulse forming capacitance the peak current and the energy per pulse increased but pulse repetition rate decreased proportionately resulting in almost the same total power dissipated in the spark gap + sliding discharge. This is expected since the input voltage, and consequently, the output voltage of the Cockcroft–Walton circuit remained constant, and hence the input power was kept the same during these experiments.

When the charging capacitance of 420pF was used, a uniform sliding discharge was observed using the 5HVS electrode assembly, as shown in Fig. 6a. No significant difference was observed in either the discharge or the voltage and current waveforms when the charging capacitance was increased from 420 to 495pF. However, further increase of the capacitance to 700pF caused localized glow-to-arc-like transition at some points in the discharge gap as shown in Fig. 6b. Such transition was accompanied with a sudden voltage drop and a sharp increase in the discharge current, indicating the development of an unsteady state (abnormal glow or arc formation).

When a 3HVS electrode assembly having capacitance ~ 45 pF was employed, the effect of the charging capacitance (C_{CH}) was similar, except that the repeatable pulsed mode was observed for capacitances greater than $C_{CH} = 150$ pF and unsteady transition started at $C_{CH} = 420$ pF. The glow-to-arc-like transition for a charging capacitance of 420pF was not observed when a 500 Ω resistor was installed in parallel to the electrode assembly. It should be mentioned that the addition of the parallel resistor decreased the energy per pulse by 10 % but there was no observable change in the peak voltage or the pulse duration (FWHM).

The addition of the 500 Ω resistor in parallel to the electrode assembly helps stabilize the discharge and prevents the localized unsteady transition. This is mainly due to the reduced voltage pulse durations, as the fall time of the pulse depends on the product of the equivalent capacitance and the resistance. In addition, current sharing by the parallel resistor also helps limit the current flow through the reactor and hence prevents the glow-to-arc transition. Therefore, for the following studies, a charging capacitance of 420pF

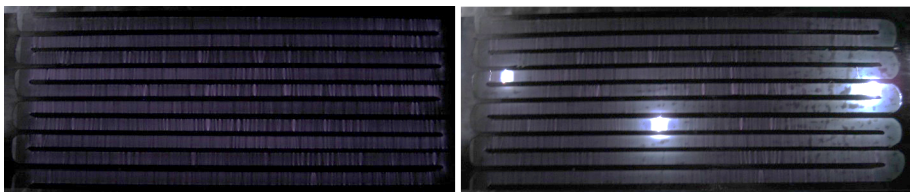


Fig. 6 Time integrated image of the plasma in 5HVS electrode assembly for $C_{CH} = 420$ pF (*left*) and for $C_{CH} = 700$ pF showing sparking at three brighter spots (*right*)

without the parallel resistor for the 5HVS electrode assembly was employed, whereas the same capacitance value but with 500 Ω parallel resistor was used for the case of 3HVS.

Effect of Spark Gap Distance

Figure 7 shows that with a gradual increase in the spark gap distance from 0.95 to 3.2 mm, the pulse repetition rate gradually decreases from ~ 300 to ~ 40 Hz. The energy per pulse shows a linear increase from ~ 5 to ~ 30 mJ with the increase in the spark gap distance. The energy per pulse increases because both peak voltage and peak current increase with an increase in the spark gap. The maximum voltage at the charging capacitor before sparking (V_2) remains about two times the peak voltage of the pulse delivered to the electrode assembly (V_3) as shown in Fig. 7b. These were single pulses, equally spaced in time like those shown in Fig. 5f for the spark gap range of 0.95–3.2 mm. However, when the spark gap distance was decreased to less than 0.95 mm, there were bursts of pulses in every discharge event like those shown in Fig. 5b.

Ozone Synthesis from Air and Oxygen

Figure 8a shows results of ozone synthesis from an air feed. Two different electrode assemblies i.e., 3HVS and 5HVS, with or without a 500 Ω parallel resistor as load were employed in this study. Gradually varying air or oxygen flow rate in the range 0.45–2.3L/min varied the specific input energy, keeping all other experimental conditions the same. For the 5HVS electrode assembly and air feed, the ozone concentration was almost the same with and without the parallel resistor for the same specific input energy conditions. The energy yield for ozone calculated from the data shown in Fig. 8a for the case of 5HVS was 80–40 g/kWh, i.e., ~ 80 g/kWh for the lowest concentration and gradually decreasing to ~ 40 g/kWh for the highest concentration in this set of experiments. The ozone concentration increased with an increase in the specific input energy but at the cost of less energy yield. Replacing the 5HVS electrode assembly with the 3HVS electrode assembly resulted in less ozone concentration for the same specific input energy. The energy yield for ozone calculated from the data shown in Fig. 8a for the case of 3HVS was ~ 50 g/kWh

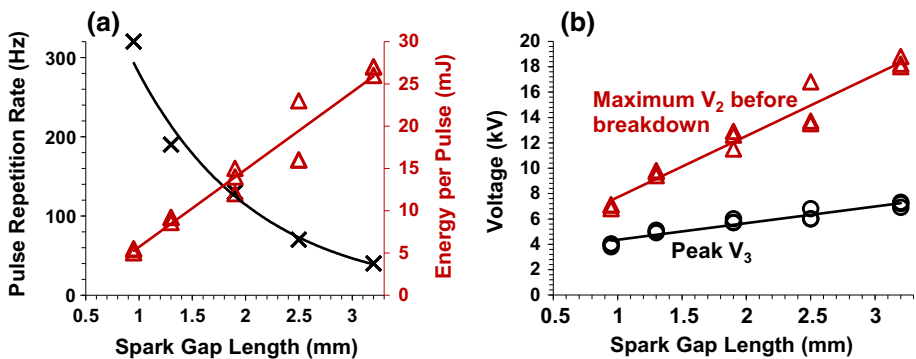


Fig. 7 Pulse repetition rate and energy per pulse versus spark gap distance curves (a) and peak voltage of the pulse (V_3) and maximum voltage before breakdown at the charging capacitor (V_2) versus spark gap distance curves (b). Conditions: 12 V input, load = 5HVS electrode assembly, $C_{CH} = 420$ pF, $R_{CH} = 3.3$ M Ω

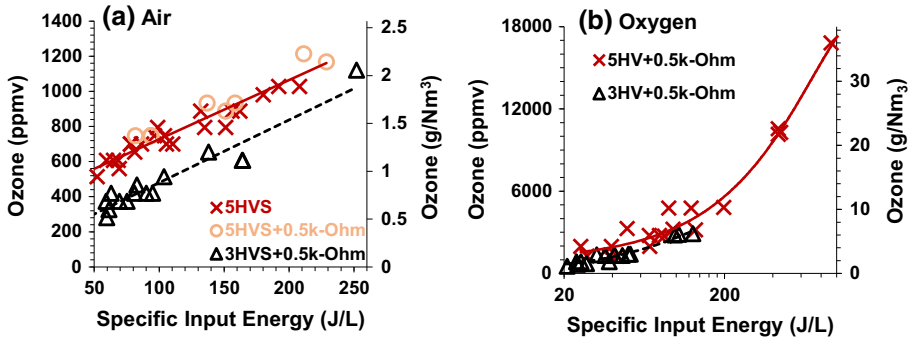


Fig. 8 Ozone concentration versus specific input energy curves for air (a) and oxygen (b) feed. Conditions: 12 V input, spark gap = 3.2 mm in the case of air and 0.9 mm in the case of oxygen, load = 5HVS, 5HVS with 500 Ω parallel resistor, or 3HVS with 500 Ω parallel resistor, $C_{CH} = 420\text{pF}$, $R_{CH} = 3.3\text{ M}\Omega$

for the lowest concentration and gradually decreased to $\sim 25\text{ g/kWh}$ for the highest concentration in this set of experiments.

The reactor that was used in the previous experiments for ozone synthesis from air was left running for $\sim 10\text{ h}$ at a time. The results in Fig. 9 show the ozone level remained almost stable during this time. The reactor was switched OFF for $\sim 14\text{ h}$, and was restarted again without cleaning the electrodes of the spark gap switch. This process was repeated for five consecutive periods (in this case 5 days). Figure 9 shows that the system can be used over a prolonged period of time with only a slight decrease in the output ozone level ($<10\%$) after 5 days of operation. Cleaning the electrodes of the switch with fine sand paper restored it to its initial performance. The low erosion rate is explained by the fact that the discharge in the switch does not have sufficient time to thermalize due to the short duration of the voltage pulse ($\sim 10\text{ ns}$) [53], so it remains a transient spark discharge which causes significantly less erosion of the electrodes compared to a spark discharge.

Figure 8b shows the results of ozone synthesis from oxygen feed. It can be observed that the ozone concentration was significantly higher with oxygen feed (Fig. 8b) as compared with air feed (Fig. 8a) for the same specific input energy. The energy yield for ozone synthesis calculated from the data shown in Fig. 8b was $\sim 230\text{ g/kWh}$ for 20 J/L and gradually decreased to $\sim 170\text{ g/kWh}$ for 120 J/L in the case of 3HVS. Similarly, the

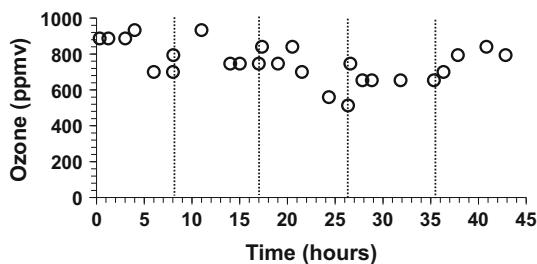
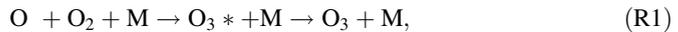


Fig. 9 Ozone concentration versus reactor operation time curve. Conditions: feed = air @ 11pm, input voltage = 12 V, spark gap = 3.2 mm, load = 5HVS with 500 Ω parallel resistor, $C_{CH} = 420\text{pF}$, $R_{CH} = 3.3\text{ M}\Omega$, specific input energy = $117 \pm 7\text{ J/L}$, energy per pulse = $12 \pm 1\text{ mJ}$, pulse repetition rate = $160 \pm 10\text{ Hz}$. The reactor was run $\sim 10\text{ h}$, switched OFF for the next 14 h and re-started at the points shown with dotted lines

energy yield was ~ 230 g/kWh for 20 J/L and gradually decreased to ~ 360 g/kWh for 120 J/L and to ~ 120 g/kWh for ~ 1000 J/L in the case of 5HVS.

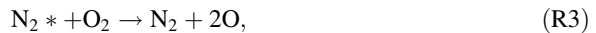
Another difference observed between the air and oxygen cases was that sparking as shown in Fig. 6 (right) was observed in the case of oxygen for spark gap ≥ 1.3 mm. The surface plasma leaves ions behind on the surface. The ions deposited on the surface were apparently more conductive in the case of pure oxygen than in the case of air which most likely resulted in the sparking. Therefore, the spark gap = 0.95 mm was employed along with the 500 Ω resistor in parallel to the electrode assembly 3HVS or 5HVS in all experiments involving pure oxygen feed.

The mechanism of ozone synthesis is described briefly in the following. Any free electron present in the strong electric field region is accelerated under the influence of the strong electric fields when the pulsed high voltage is applied to the anode. The high energy electrons ultimately collide with ambient gas molecules and may result in excitation, ionization or dissociation of the target molecules. For example, oxygen and nitrogen molecules dissociate into atomic oxygen and atomic nitrogen, respectively. Ozone is primarily produced by the following reaction [22, 57, 58]:



where * represents the excited state and M is a third collision partner that can be O_2 , N_2 , etc. Part of the ozone goes to waste due to thermal decomposition and through reactions with other species in the plasma [59, 60].

The reactive nitrogen species produce additional O atoms needed for the ozone formation through reactions such as the following [59]:



However, some of the reactive species, particularly NO, destroy a major portion of the ozone, e.g., through the following cyclic reactions [58–60]:



It explains why the ozone concentration was higher in the case of pure oxygen than in the case of the air feed. It also explains why ozone concentration increased with an increase in the specific input energy, but at the expense of lower energy yield. Multiple factors affect the final ozone yield [23]. The temperature in the plasma channels (which is usually significantly higher compared to the ambient gas) is identified as one of the major factor responsible for destroying ozone [61, 62]. Applying a lower voltage reduces the heating, but, at the same time, reduces the energy density, resulting in a higher energy yield for the lower overall ozone concentration as observed in this study.

The number of plasma channels in the case of surface plasma in this study are approximately proportional to the length of the high voltage electrode (anode in this case) [24]. Therefore, when the inter-electrode gap was reduced from 6.4 to 3.2 mm, the number of high voltage electrode strips could be increased from 3 (in the case of 3HVS) to 5 (in the case of 5HVS). It resulted in less energy per plasma channel in the later case due to the distribution of the same total energy per pulse in a larger number of plasma channels in the

case of 5HVS compared to the case of 3HVS. Further, the peak voltage of the pulse was 2–3 kV less in the case of 5HVS for the same input voltage of 12 V and for nearly the same energy per pulse compared to the case of 3HVS. Less energy per plasma channel results in less heating and minimizes the rate of ozone destruction. It explains the higher ozone concentration and higher energy yield for the same specific input energy in the case of 5HVS compared to 3HVS as observed in this study.

The energy yield for ozone synthesis from air feed was 70–40 g/kWh for specific input energy of 50–230 J/L which is almost the same as observed in our earlier studies using a commercially available pulsed power supply and the same plasma reactor system [24, 63]. These values are comparable to the values reported in earlier literature for different types of non-thermal plasmas, e.g., 110–10 g/kWh in the case of pulsed corona discharge [64–66], 100–10 g/kWh in the case of surface-DBD and coupled surface-DBD [55, 67, 68], and ~ 60 g/kWh in the case of DBD [69]. It should be mentioned here that the examples quoted above represent the most frequently reported values for ozone energy efficiency. The values in some exceptional cases may be much higher than these, e.g., 350 g/kWh has been reported for the case of a glow discharge in dry air [70].

The energy yield for ozone synthesis from oxygen feed was 360–120 g/kWh for specific input energy 50–230 J/L which is comparable to that observed in our earlier studies using the same electrode assemblies with commercially available power supply [24, 63]. It is also comparable to studies reported in literature for other commercially available power supplies and different type of discharges. For example, ~ 85 g/kWh in a surface DBD formed in microchannels in an aluminum substrate [71], 200–75 g/kWh in surface DBD with forced cooling of electrodes [61, 72] and ~ 120 g/kWh in DBD [69]. It should be mentioned that these energy yield values represent the most frequently reported results. Much higher values have also been reported in exceptional cases, e.g., 736 g/kWh reported for the case of short duration pulses (5 ns) and negative streamer mode [73]. Further, a catalyst combined with the plasma can further improve ozone yield. For example, alumina [74, 75], silica gel [76], titanium oxide [77, 78] and zinc oxide [79] are known to catalyze ozone synthesis in electrical discharges.

Conclusions

A simple low cost pulse power circuit using a Cockcroft–Walton voltage multiplier for DC charging and a spark gap for nanosecond pulsed generation was successfully employed in an ozone generator.

1. The pulse duration can be defined through the charging capacitance (C_{CH}) and the load resistance, as long as we separate the Cockcroft–Walton circuit from the load circuit through a charging resistor or an inductor. With a C_{CH} of 100pF and a load resistance of 500 Ω , pulses with decay time constants of ~ 50 ns were obtained.
2. About 80 % of the power provided to the Cockcroft–Walton circuit is accounted for by the losses in the various resistors in the pulse forming circuit, voltage probes and the load.
3. The discharge event may be followed by a burst of low voltage pulses. It can be corrected, i.e., single pulses almost equally spaced in time can be obtained, by increasing the capacitance of the charging capacitor.
4. Replacing the 500 Ω resistor load with the sliding discharge electrode assembly resulted in a decrease in voltage rise time from ~ 15 to ~ 3 ns and in full width at half

- maximum from ~ 60 to ~ 10 ns. This is due to the lower resistance ($<50 \Omega$) of the sliding discharge.
5. Ozone was produced from air and from oxygen feed in the nanosecond portable pulse generator plus sliding discharge system with an energy efficiency almost the same as reported in literature with a commercial pulse generator and the sliding discharge system. The efficiency was comparable to values often reported in literature for other types of non-thermal plasmas.
 6. The ozone generator powered by this pulse generator showed only a slight reduction in efficiency of ozone production after more than 25 million pulses. This is assumed to be due to the extremely short pulse duration which prevents thermalization of the discharge plasma, and consequently reduces electrode erosion which limits the switch lifetime.

References

1. Akiyama H, Sakugawa T, Namihira T, Takaki K, Minamitani Y, Shimomura N (2007) Industrial applications of pulsed power technology. *IEEE Trans Dielectr Electr Insul* 14(5):1051–1064
2. Kogelschatz U (2004) Atmospheric-pressure plasma technology. *Plasma Phys Controll Fusion* 46(12B):B63
3. Malik MA, Malik SA (1999) Pulsed corona discharges and their applications in toxic VOCs abatement. *Chin J Chem Eng* 7(4):351–362
4. Vandembroucke AM, Morent R, De Geyter N, Leys C (2011) Non-thermal plasmas for non-catalytic and catalytic VOC abatement. *J Hazard Mater* 195:30–54
5. Preis S, Klauson D, Gregor A (2013) Potential of electric discharge plasma methods in abatement of volatile organic compounds originating from the food industry. *J Environ Manag* 114:125–138
6. Beckers FJCM, Hoeben WFLM, Huiskamp T, Pemen AJM, van Heesch EJM (2013) Pulsed corona demonstrator for semi-industrial scale air purification. *IEEE Trans Plasma Sci* 41(10):2920–2925
7. Mizuno A (2013) Generation of non-thermal plasma combined with catalysts and their application in environmental technology. *Catal Today* 211:2–8
8. Holub M, Brandenburg R, Grosch H, Weinmann S, Hansel B (2014) Plasma supported odour removal from waste air in water treatment plants: an industrial case study. *Aerosol Air Qual Res* 14(3):697–707
9. Thevenet F, Sivachandiran L, Guaitella O, Barakat C, Rousseau A (2014) Plasma–catalyst coupling for volatile organic compound removal and indoor air treatment: a review. *J Phys D Appl Phys* 47(22):224011
10. Masuda S, Hosokawa S, Tu X, Wang Z (1995) Novel plasma chemical technologies—PPCP and SPCP for control of gaseous pollutants and air toxics. *J Electrostat* 34(4):415–438
11. Penetrante BM, Brusasco RM, Merritt BT, Vogtlin GE (1999) Environmental applications of low-temperature plasmas. *Pure Appl Chem* 71(10):1829–1835
12. Hammer T (2014) Atmospheric pressure plasma application for pollution control in industrial processes. *Contrib Plasma Phys* 54(2):187–201
13. Talebizadeh P, Babaie M, Brown R, Rahimzadeh H, Ristovski Z, Arai M (2014) The role of non-thermal plasma technique in NOx treatment: a review. *Renew Sustain Energ Rev* 40:886–901
14. Kelly-Wintenberg K, Sherman DM, Tsai PY, Gadri RB, Karakaya F, Chen Z, Roth JR, Montie TC (2000) Air filter sterilization using a one atmosphere uniform glow discharge plasma (the volfilter). *IEEE Trans Plasma Sci* 28(1):64–71
15. Park CW, Byeon JH, Yoon KY, Park JH, Hwang J (2011) Simultaneous removal of odors, airborne particles, and bioaerosols in a municipal composting facility by dielectric barrier discharge. *Sep Purif Technol* 77(1):87–93
16. Wu Y, Liang Y, Wei K, Li W, Yao M, Zhang J (2014) Rapid allergen inactivation using atmospheric pressure cold plasma. *Environ Sci Technol* 48(5):2901–2909
17. Zhou P, Yang Y, Lai AC, Huang G (2016) Inactivation of airborne bacteria by cold plasma in air duct flow. *Build Environ*
18. Malik MA, Ghaffar A, Malik SA (2001) Water purification by electrical discharges. *Plasma Sources Sci Technol* 10(1):82

19. Locke BR, Sato M, Sunka P, Hoffmann MR, Chang JS (2006) Electrohydraulic discharge and non-thermal plasma for water treatment. *Ind Eng Chem Res* 45(3):882–905
20. Malik MA (2010) Water purification by plasmas: which reactors are most energy efficient? *Plasma Chem Plasma Process* 30(1):21–31
21. Banaschik R, Burchhardt G, Zocher K, Hammerschmidt S, Kolb JF, Weltmann KD (2016) Comparison of pulsed corona plasma and pulsed electric fields for the decontamination of water containing *Legionella pneumophila* as model organism. *Bioelectrochemistry*. doi:10.1016/j.bioelechem.2016.05.006
22. Wojtowicz JA (2005) Ozone. *Kirk-Othmer Encycl Chem Technol*. doi:10.1002/0471238961.1526151423151020.a01.pub2
23. Jodzis S, Patkowski W (2016) Kinetic and energetic analysis of the ozone synthesis process in oxygen-fed DBD reactor. Effect of power density, gap volume and residence time. *Ozone Sci Eng* 38(2):86–99
24. Malik MA, Hughes D (2016) Ozone synthesis improves by increasing number density of plasma channels and lower voltage in a nonthermal plasma. *J Phys D Appl Phys* 49(13):135202
25. Vasilets VN, Shekhter AB (2012) Nitric oxide plasma sources for bio-decontamination and plasma therapy. In: *Plasma for bio-decontamination, medicine and food security*, Springer Netherlands, pp 393–402
26. Suschek CV, Opländer C (2016) The application of cold atmospheric plasma in medicine: the potential role of nitric oxide in plasma-induced effects. *Clin Plasma Med* 4(1):1–8
27. Edelblute CM, Malik MA, Heller LC (2016) Antibacterial efficacy of a novel plasma reactor without an applied gas flow against methicillin resistant *Staphylococcus aureus* on diverse surfaces. *Bioelectrochemistry*. doi:10.1016/j.bioelechem.2016.04.001
28. Sakai S, Matsuda M, Wang D, Namihira T, Akiyama H, Okamoto K, Toda K (2009) Nitric oxide generator based on pulsed arc discharge. *Acta Phys Polonica-Series Gen Phys* 115(6):1104
29. Yu B, Muenster S, Blaesi AH, Bloch DB, Zapol WM (2015) Producing nitric oxide by pulsed electrical discharge in air for portable inhalation therapy. *Sci Transl Med* 7(294):294ra107
30. Malik MA (2016) Nitric oxide production by high voltage electrical discharges for medical uses: a review. *Plasma Chem Plasma Process* 36(3):737–766
31. Schoenbach KH, Nuccitelli R, Beebe SJ (2006) Zap [extreme voltage for fighting diseases]. *IEEE Spectr* 43(8):20–26
32. Connolly RJ, Hoff AM, Gilbert R, Jaroszeski MJ (2015) Optimization of a plasma facilitated DNA delivery method. *Bioelectrochemistry* 103:15–21
33. Edelblute CM, Heller LC, Malik MA, Bulysheva A, Heller R (2016) Plasma-activated air mediates plasmid DNA delivery in vivo. *Mol Ther Methods Clin Dev* 3:16028
34. Williamson JM, Trump DD, Bletzinger P, Ganguly BN (2006) Comparison of high-voltage ac and pulsed operation of a surface dielectric barrier discharge. *J Phys D Appl Phys* 39(20):4400–4406
35. Zhang X, Lee BJ, Im HG, Cha MS (2016) Ozone production with dielectric barrier discharge: effects of power source and humidity. *IEEE Trans Plasma Sci*, in press
36. Rosocha LA (2005) Nonthermal plasma applications to the environment: gaseous electronics and power conditioning. *IEEE Trans Plasma Sci* 33(1):129–137
37. Chiper AS, Blin-Simiand N, Heninger M, Mestdagh H, Boissel P, Jorand F, Lemaire J, Leprovost J, Pasquiers S, Popa G, Postel C (2010) Detailed characterization of 2-heptanone conversion by dielectric barrier discharge in N₂ and N₂/O₂ mixtures. *J Phys Chem A* 114(1):397–407
38. Spaan M, Leistikow J, Schulz-Von Der Gathen V, Döbele HF (2000) Dielectric barrier discharges with steep voltage rise: laser absorption spectroscopy of NO concentrations and temperatures. *Plasma Sources Sci Technol* 9(2):146
39. Puchkarev V, Gundersen M (1997) Energy efficient plasma processing of gaseous emission using a short pulse discharge. *Appl Phys Lett* 71(23):3364–3366
40. Jiang C, Lane J, Song S, Pendelton SJ, Wu Y, Sozer E, Kuthi A, Gundersen MA (2016) Single-electrode He microplasma jets driven by nanosecond voltage pulses. *J Appl Phys* 119(9):083301. doi:10.1063/1.4942624
41. Namihira T, Tsukamoto S, Wang D, Katsuki S, Hackam R, Akiyama H, Uchida Y, Koike M (2000) Improvement of NO_x removal efficiency using short-width pulsed power. *IEEE Trans Plasma Sci* 28(2):434–442
42. Matsumoto T, Wang D, Namihira T, Akiyama H (2011) Process performances of 2 ns pulsed discharge plasma. *Jpn J Appl Phys* 50(8S1):08JF14
43. Namihira T, Wang D, Akiyama H (2009) Pulsed power technology for pollution control. *Acta Phys Pol A* 115(6):953–955

44. Carman RJ, Mildren RP, Ward BK, Kane DM (2004) High-pressure (>1 bar) dielectric barrier discharge lamps generating short pulses of high-peak power vacuum ultraviolet radiation. *J Phys D Appl Phys* 37(17):2399
45. Jiang WH, Yatsui K, Takayama K, Akemoto M, Nakamura E, Shimizu N, Tokuchi A, Rukin S, Tarasenko V, Panchenko A (2004) Compact solid-state switched pulsed power and its applications. *Proc IEEE* 92:1180–1196
46. Kuffel E, Zaengl W, Kuffel J (2000) *High voltage engineering: fundamentals*, 2nd ed, Newnes, Woburn, MA 13–21, ISBN 0 7506 3634 3
47. Greinacher H (1921) Über eine Methode, Wechselstrom mittels elektrischer Ventile und Kondensatoren in hochgespannten Gleichstrom umzuwandeln. *Zeitschrift für Physik* 4(2):195–205
48. Cockcroft JD, Walton ETS (1930) Experiments with high velocity positive ions. In: *Proceedings of the royal society of London. Series A, containing papers of a mathematical and physical character*, 477–489
49. Young CM, Chen MH, Chang TA, Ko CC, Jen KK (2013) Cascade Cockcroft–Walton voltage multiplier applied to transformerless high step-up DC–DC converter. *IEEE Trans Ind Electron* 60(2):523–537
50. Potturi VR, Malik MA, Schoenbach KH, Jiang C (2014) Low cost, multi-kilohertz pulse generator for non-equilibrium plasma-based air purification. In: *Power modulator and high voltage conference (IPMHVC), 2014 IEEE international IEEE 49–52*
51. Müller L, Kimball JW (2016) High gain DC–DC converter based on the Cockcroft–Walton multiplier. *IEEE Trans Power Electron* 31(9):6405–6415
52. Katzir L, Shmilovitz D (2016) A split-source multisection high-voltage power supply for x-ray. *IEEE J Emerg Sel Top Power Electron* 4(2):373–381
53. Janda M, Machala Z, Niklová A, Martišovits V (2012) The streamer-to-spark transition in a transient spark: a dc-driven nanosecond-pulsed discharge in atmospheric air. *Plasma Sour Sci Technol* 21(4):045006
54. Malik MA, Hughes D, Heller R, Schoenbach KH (2015) Surface plasmas versus volume plasma: energy deposition and ozone generation in air and oxygen. *Plasma Chem Plasma Process* 35(4):697–704
55. Malik MA, Schoenbach KH, Heller R (2014) Coupled surface dielectric barrier discharge reactor-ozone synthesis and nitric oxide conversion from air. *Chem Eng J* 256:222–229
56. Abdel-Salam M, Anis H, El-Morshedy A, Radwan R (2000) *High voltage engineering—theory and practice*, (2nd ed) Marcel Dekker Inc., New York, pp 531–535, ISBN# 0-8247-0402-9
57. Kogelschatz U, Eliasson B, Hirth M (1988) Ozone generation from oxygen and air: discharge physics and reaction mechanisms. *Ozone Sci Eng* 10:367–378
58. Jodzis S (2011) Application of technical kinetics for macroscopic analysis of ozone synthesis process. *Ind Eng Chem Res* 50:6053–6060
59. Kogelschatz U, Baesaler P (1987) Determination of nitrous oxide and dinitrogen pentoxide concentrations in the output of air-fed ozone generators of high power density. *Ozone Sci Eng* 9:195–206
60. Yehia A (2012) Assessment of ozone generation in dry air fed silent discharge reactors. *Phys Plasmas* 19:023503
61. Jodzis S (2012) Effective ozone generation in oxygen using a mesh electrode in an ozonizer with variable linear velocity. *Ozone Sci Eng* 34:378–386
62. Jodzis S (2013) Temperature effects under ozone synthesis process conditions. *Eur Phys J Appl Phys* 61:24319
63. Malik MA (2014) Ozone synthesis using shielded sliding discharge: effect of oxygen content and positive versus negative streamer mode. *Ind Eng Chem Res* 53(31):12305–12311
64. Samaranyake WJM, Miyahara Y, Namihira T, Katsuki S, Sakugawa T, Hackam R, Akiyama H (2000) Pulsed streamer discharge characteristics of ozone production in dry air. *IEEE Trans Dielectr Electr Insul* 7:254–260
65. Simek M, Clupek M (2002) Efficiency of ozone production by pulsed positive corona discharge in synthetic air. *J Phys D Appl Phys* 35:1171–1175
66. Ikemoto T, Ninomiya T, Morimoto M, Teranishi K, Shimomura N (2015) Investigation of electrode structure for dense ozone production using nanosecond pulsed powers. In: *IEEE pulsed power conference (PPC) 1–4* DOI:[10.1109/PPC.2015.7296874](https://doi.org/10.1109/PPC.2015.7296874)
67. Pekarek S (2012) Experimental study of surface dielectric barrier discharge in air and its ozone production. *J Phys D Appl Phys* 45:075201
68. Simek M, Pekarek S, Prukner V (2012) Ozone production using a power modulated surface dielectric barrier discharge in dry synthetic air. *Plasma Chem Plasma Process* 32:743–754
69. Yao S, Wu Z, Han J, Tang X, Jiang B, Lu H, Yamamoto S, Kodama S (2015) Study of ozone generation in an atmospheric dielectric barrier discharge reactor. *J Electrostat* 75:35–42

70. Buntat Z, Smith IR, Razali NA (2009) Ozone generation using atmospheric pressure glow discharge in air. *J Phys D Appl Phys* 42:235202
71. Kim MH, Cho JH, Ban SB, Choi RY, Kwon EJ, Park SJ, Eden JG (2013) Efficient generation of ozone in arrays of microchannel plasmas. *J Phys D Appl Phys* 46:305201
72. Simek M, Pekarek S, Prukner V (2010) Influence of power modulation on ozone production using an AC surface dielectric barrier discharge in oxygen. *Plasma Chem Plasma Process* 30:607–617
73. Takamura N, Matsumoto T, Wang D, Namihira T, Akiyama H (2011) Ozone generation using positive- and negative-nanoseconds pulsed discharges. In: *IEEE pulsed power conference (PPC)*, 1300–1303
74. Huang W, Ren T, Xia W (2007) Ozone generation by hybrid discharge combined with catalysis. *Ozone Sci Eng* 2:107–112
75. Chen HL, Lee HM, Chang MB (2006) Enhancement of energy yield for ozone production via packed-bed reactors. *Ozone Sci Eng* 28:111–118
76. Jodzis S (2003) Effect of silica packing on ozone synthesis from oxygen–nitrogen mixtures. *Ozone Sci Eng* 25:63–72
77. Pekárek S (2015) Effect of TiO₂ and reverse air supply on ozone production of negative corona discharge with the needle in the dielectric tube to mesh electrode system. *Plasma Chem Plasma Process* 35(4):705–719
78. Pekárek S, Mikeš J, Pelikánová IB, Krčma F, Dzik P (2016) Effect of TiO₂ on various regions of active electrode on surface dielectric barrier discharge in air. *Plasma Chem Plasma Process*. doi:[10.1007/s11090-016-9723-4](https://doi.org/10.1007/s11090-016-9723-4)
79. Pekárek S, Mikeš J, Krýsa J (2015) Comparative study of TiO₂ and ZnO photocatalysts for the enhancement of ozone generation by surface dielectric barrier discharge in air. *Appl Catal A Gen* 502:122–128